Tikrit Journal of Pure Science 21 (6) 2016 *ISSN: 1813 – 1662 (Print)*
E-ISSN: 2415 – 1726 (On Line)

Structural, Mossbauer spectra and magnetic properties of $Ni_{(1-x)}$ Cd_x Fe_2O_4 by solid state Reaction method

Abdulsamee Fawzi Abdul Aziz Al-Bayati
Natural Ressources Research Center , Tikrit University , Tikrit , Iraq
abdulsamee_fawzi@yahoo.com

Abstract
The preparation of Ni-Cd ferrite having the chemical formula $Ni_{(1-x)}Cd_xFe_2O_4$ where x varies from 0, 0.1, 0.2, 0.3, 0.4, and 0.5 were synthesized by solid state reaction method. The X-ray analysis shows the existence of single phase spinel structure with increase of lattice parameter and density with increasing Cd contents were as the porosity decreases. The particle size was calculated by X-ray broadening studies. The Vickers hardness of Ni-Cd ferrite system variation between 532 to 568.6. The increase in hardness of composites results from increased Cd-content. The Atomic Force Microscopy (AFM) showed that the average grain size was increases with the increase in Cd content. The variation of dielectric constant, loss tangent and AC conductivity as a function of frequency in frequency range 100Hz-5MHz was studied. The dielectric constants decreases with increasing frequency for all the samples and follow the Maxwell-Wagner's interfacial polarization. The Hall coefficient was found to be positive. It demonstrates that the majority of charge carriers of p-type. The magnetic properties of $Ni_{(1-x)}Cd_xFe_2O_4$ ferrites were strongly affected by the Cd content. The Mossbaure spectra show canted spin structure for all the samples.

Key words: X-ray diffraction; Electron microscopy; Dielectric constant; Hysteresis loop.

1. Introduction
Ni-ferrite ($NiFe_2O_4$)with high coercively is promising for various magnetic applications such as magnetic recording and magneto-optical devices because of its stable ferromagnetic transition temperature, relatively high saturation magnetization, high magnetostriction, good chemical stability and high resistance [1]. In ferrites, the magnetic ions occupy the tetrahedral (A) and octahedral (B) sites of the spinel structure. The exchange integrals (J_{AB}, J_{BB}, and J_{AA}) are generally negative and the antiferromagnetic interaction A–B is stronger than B–B and A–A interactions [2]. This leads to ferrimagnetism: B–B and A–A interactions being frustrated, the spins of magnetic ions in the same sub lattice are parallel and those of the two sub lattices are antiparallel. cadmuim being nonmagnetic element, substitution in Ni ferrite enhances the magnetization and hence magnetostrictive properties of the ferrite, reduces the curie temperature, affects on electrical properties of ferrites. Hence, the samples of $Ni_{(1-x)}Cd_{(x)}Fe_2O_4$, with x=(0-0.5) have been synthesized. Substitution of Cd above x = 0.5 reduces the magnetic and magnetostrictive properties, therefore, the composition with x > 0.5 were not used in the present studies. Synthesis of nanocrystalline ferrite using various chemical methods is well known [3,4]. However, reduction in size of magnetic particles reduces the magnetic and hence magnetostrictive properties of the ferrites. On the other hand synthesis of ferrites using solid state reaction technique results in formation of microcrystalline samples. The microcrystalline ferrite possesses superior magnetic and magnetostrictive properties than that of nano crystalline samples. Hence, in the present work, $Ni_{(1-x)}Cd_xFe_2O_4$ samples, where x = 0, 0.1, 0.2, 0.3, 0.4 and 0.5 named as A, B, C, D, E and F respectively have been prepared by the solid state reaction method. In order to explain the results obtained from the dielectric measurements, have also performed in filed Mossbauer spectroscopy, extended x-ray absorption fine structure (EXAFS) and magnetization measurement.

2. Experimental
The Ni-Cd ferrites were prepared using the solid state reaction method. The powders of NiO, CdO and Fe_2O_3 in the required stoichiometric proportion were thoroughly mixed and milled for 3-4 hours. The second stage is pre-sintering, which involves heating of intimate mixture of raw materials in order to start reaction between initial ingredients. The pre-sintering helps in homogenization, to remove the absorbed gases and moisture, causes partial reaction of the oxides and tends to reduce the shrinkage during the final sintering. The powders were pre-sintered at 900 ^oC for 24 hours. The pre sintered powders were then milled to fine powder so as to reduce the particle size and to promote mixing of any unreacted oxides. These powders were then mixed with 1% polyvinyl alcohol as a binder and pressed into pellets having diameter of 10 mm and thickness of 2-3 mm using hydraulic press by applying a pressure of 4 tones/inch for 10 min.. The samples in the form of pellet were sintered at 1200^oC for 12 hours. The sintering involves large scale diffusion and erasing of gradients of chemical potentials, resulting in formation of product. The flow chart of preparation is shown in Fig. 1.

ISSN: 1813 – 1662 (Print)
E-ISSN: 2415 – 1726 (On Line)

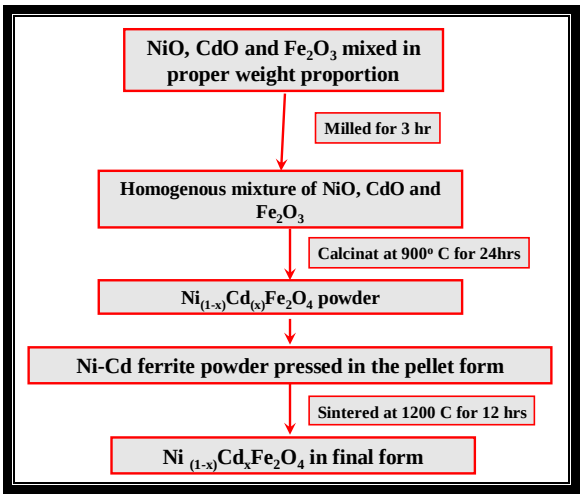

Fig. 1. Flow chart for synthesis of $Ni_{1-x}Cd_xFe_2O_4$samples

The x-ray diffraction patterns of all the samples were recorded using x-ray diffracto- meter (model Bruker D8 Advance), with CuKα radiations (λ=1.5418 Å) at a scanning rate of 0.4 sec/step. The angle at which maximum intensity lines. The Bragg angle was noted carefully and used for the determination at crystallographic parameter. Methods, of detailed analysis of crystallographic parameter could be found in lateralize. The peak angles of XRD pattern for all the samples were carefully indexed and cell parameters.

The lattice constant 'a' and the Miller indices (hkl) of reflecting planes are related by the equation [5].

$$d = \frac{a}{\sqrt{h^2 + k^2 + l^2}} \text{ ---------- (1)}$$

Substituting the values of'd' in equation (1) can calculate the lattice constant 'a'.

The average particle size (D_p) of the samples is calculated using Scherrer's equation [6].

$$D_p = \frac{k\lambda}{\beta \cos \theta} \text{ ---------- (2)}$$

where k = 0.89 (assuming the particles are spherical in shape); λ = wavelength of X-ray wavelength; β = full width at half maximum (FWHM) of the diffraction peak; and θ = angle of diffraction. The X-ray density of the ferrite and ferroelectric was calculated using the formula [7],

$$\rho_1 = 8M / Na^3 \text{ ------- (3)}$$

where, M is molecular weight expressed in grams, and N is Avogadro's number (6.023 x 10^{23} molecule / mole).

The actual density of the samples can be calculated using Hendrick and Adams method [8].The method depends upon the weight of the sample in air and weight in a liquid of known density in which the sample is insoluble. In the present studies Xylene was used as liquid in which ferrite/ ferroelectric/ composite sample were immersed. For these samples Xylenes (ρ =0.861 g/cm^3 at 20^{0}C) was used. The actual density (ρ_a) was calculated using the formula

$$\rho_a = \frac{Weight\ of\ sample\ in\ air}{Weight\ of\ sample\ in\ air - Weight\ in\ xylene} \times density\ of\ xylene \text{ ----- (4)}$$

$$\rho_a = \frac{W_{air}}{W_{air} - W_{xylene}} \times \rho_{xylene}$$

The porosity was calculated from the relation [9].

$$\text{Percentage porosity} = \left\{\frac{100\,(\rho_x - \rho_a)}{\rho_x}\right\} \% \text{ ----- (5)}$$

Atomic Force Microscope (JEOL, Analytical Microscopy Model Atomic Force Microscope JSM – 6360A) was used to obtain the microstructure and elemental analysis of the composites. Average grain size (grain diameter) of the sample was determined from AFM and Optical microscope (OP) micrographs by linear-intercept technique [10].

Hardness is defined as the resistance of the material to deformation. The Vickers hardness is obtained by dividing the applied load by the surface area of the indentation, according to the equation

$$HV = P/A = 1.8544P/d^2 \text{ ….. (6)}$$

where P is the applied load in Kg, A is the surface area of the indentation in mm^2 and d is the mean diagonal length in millimeters [11].This test is an indentation test which forces a square-based pyramidal-shaped diamond indenter, having a face angle of 140^o, into the surface of the materials to be tested. For the measurement of Vickers hardness, a smooth sample surface is required, therefore the A, B, C, D, E, F and G samples. The final polishing was carried out by a paste of 0.5 μm alumina powder in acetone on the paper (800 NP5grit).

The ^{57}Fe Mossbauer spectra were recorded at 77 K with zero external magnetic fields and at 10 k with 8T external field applied parallel to the γ-beam. The EXAFS measurments were done using laboratory x-ray absorption spectrometere (Rigaku R-XAS Lopper) at NiK (8332 eV) and Znk (9663 eV) absorption edges designed at department of physics, Pune university, Pune- India.

The dielectric measurements were carried out in the wide range of frequency measurements viz. 100 Hz to 5 MHz at room temperature and at four fixed frequencies viz. 1 kHz, 10 kHz, 100 kHz and 1 MHz in the wide range of temperature measurments using LCR Meter Bridge (model HIOKI 3532-50 LCR Hi TESTER). The dielectric constant (έ) was calculated by using the formula [12].

$$\varepsilon' = \frac{C_p \times d}{\varepsilon_o A} \text{ ------ (7)}$$

where C_p is parallel plate capacitance in pico-farad, d is thickness of the pellet in cm, A is area of cross section of pellet = π r^2 (r is radius of the pellet in cm) and ε_o is constant of permittivity of free space (ε_o = 8.85*10^{-12} F/cm). The varation of dielectric constant and loss tangent with temperature was studied at four fixed frequencies viz. 1 kHz, 10 kHz, 100 kHz and 1 MHz, by recording the same parameters.

AC conductivity is frequency and temperature dependent and is related to the dielectric relaxation caused by localized electric charge carriers. The AC conductivity of the samples was estimated from the dielectric parameters. As long as the pure charge transport mechanism is the major contributor to the loss mechanisms, the ac conductivity (σ_{ac}) may be calculated using the relation [13].

$$\sigma_{ac} = \omega \acute{\varepsilon} \varepsilon_0 \tan \delta \text{ ------- (8)}$$

Where, ε_o is the permittivity of the free space, ω is the angular frequency and tan δ is the loss tangent.

The Hall Effect properties are widely using in the interpretation of the conduction mechanism in semiconductor.

The magnetization measurements studies were carried out by using the high field hysteresis loop tracer designed at department of physics, pune university, Pune- India.

3. Results and discussion

3. 1 Structural property

The X-ray diffraction pattern of ferrite samples having general formula $Ni_{(1-x)}$ $Cd_{(x)}Fe_2O_4$ where x = 0, 0.1, 0.2, 0.3, 0.4 and 0.5 are shown in Fig. 2. All the patterns were indexed using JCPDS data for $NiFe_2O_4$, Ni-Cd ferrite card no. (10-325) (8-234) respectively, which depict cubic spinel structure of Ni-Cd ferrite samples. There are no extra peaks indicating purity of the samples synthesized. The positions of all the Bragg lines were used to obtain the interplaner spacing and these values were used to index the peaks [14].

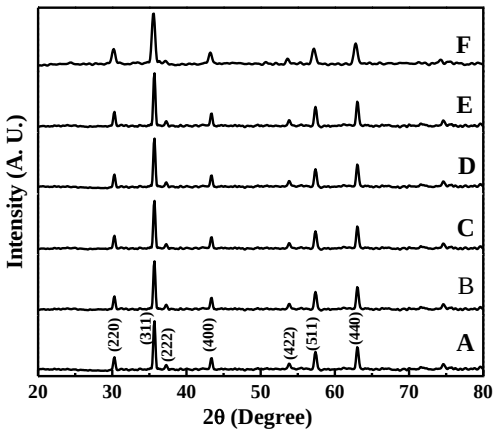

Fig. 2 X-ray diffraction patterns for A, B, C, D, E and F compositions at room tempersure.

The observed and calculated 'd' values are given in Table 1.These are in good agreement with each other for all indexed planes in case of all samples.

Table 1 Miller indices and inter planer spacing for $Ni_{(1-x)}Cd_xFe_2O_4$ ferrites.

(hkl)	$d_{std.}$	A	B	C	D	E	F
		$d_{obs.}$	$d_{obs.}$	$d_{obs.}$	$d_{obs.}$	$d_{obs.}$	$d_{obs.}$
(220)	2.9061	2.91995	2.9339	2.9280	2.9221	2.9233	2.9245
(311)	2.4938	2.49535	2.4969	2.4973	2.4977	2.49815	2.4986
(222)	2.3909	2.39645	2.402	2.3971	2.392	2.3965	2.4012
(400)	2.0731	2.07685	2.0806	2.0774	2.0742	2.0776	2.0811
(422)	1.6849	1.68865	1.6924	1.6927	1.6933	1.68915	1.6853
(511)	1.587	1.59255	1.5981	1.5981	1.5981	1.59915	1.6002

The concentration dependence of the lattice constant (a) with an accuracy of ± 0.02Å was determined form XRD data for x = 0-0.5 and given in Table 2.

It is clear from Table 2 that the doping greatly affect the lattice constant (a) for all samples obeying vegard's law [15]. Usually, in a solid solution of spinels within the miscibility range, a linear change in the lattice constant with the concentration of the components is observed [16]. The slow linear increase in the lattice constant due to the replacement of Ni^{2+} (0.74 Å) ions by slightly larger Cd^{2+} ions with an ionic radius of (0.83Å) in the system $Ni_{(1-x)}Cd_xFe_2O_4$. Similar explanation in case doped nickel ferrite is given by Abdulsamee et. al. [17]. The dependence of density ρ, X-ray density ρ_x, ρ_a and porosity P upon cadmium content x is represented in Fig. 3. The increase of diensity with Cd content can be attributed to the atomic weight and density of Cd (8.9, 112 g/cm^3) which are higher than those on Ni (8.5, 5.78 g/cm^3). The replacement of Ni^{2+} by Cd^{2+} ions in the spinel leads to a variation in bonding and consequently interatomic distance and density. The oxygen ions which diffuse though the material during sintering also accelerate the densification of the material. The apparent density of the X-ray density. The density is higher than the apparent value due to the existence of pores which depends on the sintering condition. The porosity decreases as Cd content increases which reflects the opposite behavior of density. Similar explanation in case of Co-ferrite substituted by Cd [18].

Table 2 lattice constant (a), x-ray density (ρ_x), actual density (ρ_a) and percentage porosity (p), crystalline size (t) grain size (D_t) and Vickers Hardness.

Samples	a (Å)	ρ_x gm/cm^3	ρ_a gm/cm^3	P (%)	t (nm)	VHS
A	8.34	5.210	4.880	6.33	27.73	532
B	8.36	5.213	4.929	5.45	28.29	539.2
C	8.38	5.214	4.976	4.46	30.14	546.7
D	8.39	5.215	5.012	3.61	31.51	553.5
E	8.40	5.217	5.052	2.10	34.02	560.3
F	8.41	5.218	5.090	1.85	37.21	568.6

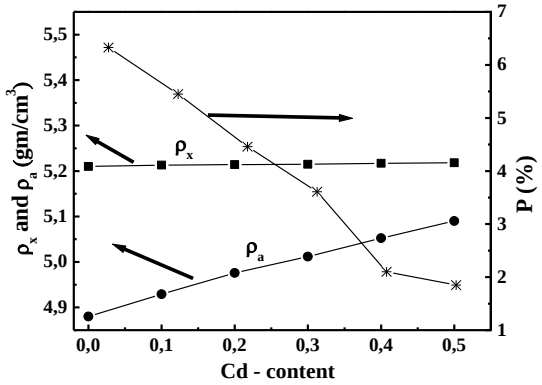

Fig. 3. X-ray density, acual density and porosity as a function of Cd-content.

The radii of the tetrahedral (R_{tetra}) and octahedral (R_{octra}) sites, the tetrahedral (R_{Ax}) and octahedral (R_{Bx}) bond length, the tetrahedral edge length (R_{xx}), the shared octahedral edge length ($R_{x'x}$), and the unshared octahedral edge length ($R_{x''x}$) of cubic mixed spinel oxides have been calculated by using the following equations [19-20].

Have been calculated by using the relation 9 (a-g) [17]

$$R_{tetra} = \sqrt{3}(u - 1/4)a - R_O \quad \text{.....(a)}$$

$$R_{octa} = \{3u^2 - (11/4)u + 43/64\}^{1/2} a - R_O \quad \text{... (b)}$$

$$R_{Ax} = \sqrt{3}(u - 1/4)a \quad \text{....(c)}$$

$$R_{Bx} = \{3u^2 - (11/4)u + 43/64\}^{1/2} a \quad \text{.. (d)}$$

$$R_{xx} = \sqrt{2}(2u - 1/2)a \quad \text{..... (e)}$$

$$R_{x'x} = \sqrt{2}(1 - 2u)a \quad \text{..... (f)}$$

$$R_{x''x} = \{4u^2 - 3u + 11/16\}^{1/2} a \quad \text{...(g)}$$

Observations from Fig. 4 indicate that with increasing Cd concentration, radius of tetrahedral site is increased whereas that of octahedral site is decreased, which in turn increases the lattice parameter.

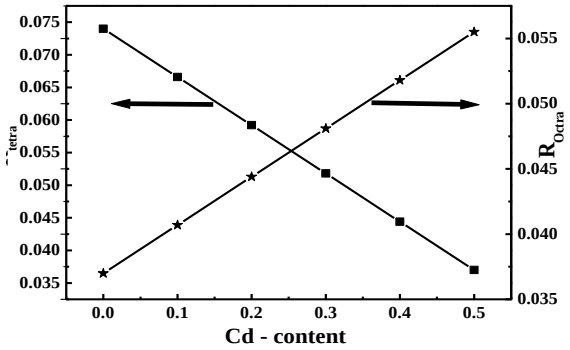

Fig. 4 represents the relation between tetrahedral site radius ($R_{tetra.}$) and octahedral sites radius ($R_{octra.}$) with the Cd-content.

clarified in Table 2. The hardness values increased when increasing the concentration of cadmium where the highest value of hardness at (x = 0.5) and the lowest value of hardness at (x = 0.0). The low value of the hardness to the reasons the nature of forming and scratch resistance while the increase back to increase bulk density, which leads to reduce the porosity of the samples prepared in a manner Technology powders and described in advance of the results of X-ray diffraction.

3.2 Mossbauer spectra analysis:

Fig. 5. Represent the room temperature Mossbauer spectra for the $Ni_{1-x}Cd_xFe_2O_4$ (x = 0.0, 0.1, 0.2, 0.3, 0.4 and 0.5) samples. It is clear from this figure that all the samples show a doublet type of Mossbauer spectra and ferromagnetic nature six line pattern of Mossbauer spectra has been observed. Some spectral broadening is also observed, which increases with increasing concentration of Cd^{2+} in the $Ni_{(1-x)}Cd_xFe_2O_4$ system. This spectral broadening is due to the changes in the tetrahedral bond length and due to the change in the Ni^{2+}, Cd^{2+} and Fe^{3+} ionic distributions in the tetrahedral and octahedral sites of this $Ni_{1-x}Cd_xFe_2O_4$ cubic spinel ferrite system. Similar explanation in case of Zn-ferrite substituted by Cd [21].

ISSN: 1813 – 1662 (Print)
E-ISSN: 2415 – 1726 (On Line)

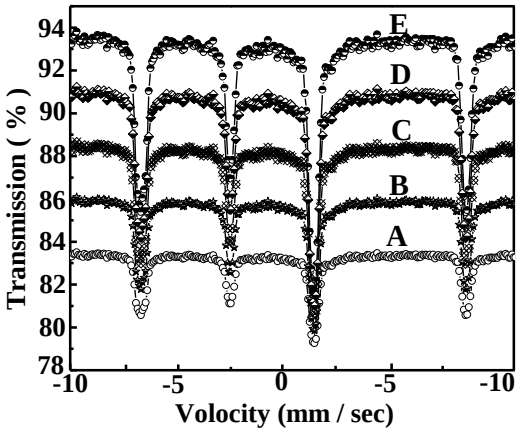

Fig. 5. Room temperature Mossbauer spectra for A, B, C, D, E and F samples.

3.3 Atomic force microscopy (AFM)

Atomic force micrographs of the samples were obtained by using Analytical PSIA Advance Scanning Probe Microscope (XE series). The atomic force micrographs of A and B samples are shown in Fig.6. It is clearly seen in the micrographs that the grains size increasing with increase Cd content. The grain size and their distribution is found to be almost uniform in the samples. The average grain size determined from AFM was noted as 30 - 50 nm for samples of the series. Atomic force microscope is used to study the topography of the surface and the surface of the crystal structure models Lafraatah, and through him can be calculated granular size (Grain size), and the rate of surface roughness (Roughness Average), and the rate of the square root (Root Mean Square). AFM has been conducting tests of A and B samples as in Fig. 6 which pictures show two-dimensional topographic analysis (2D) and three dimensions (3D) on respectively. It was found that the square root rate and the rate of surface roughness value decreases with increasing concentration of cadmium as shown in the table (3). The surface roughness rate decrease with the increase in the concentration of cadmium interpreted Enmaa crystalline granules occurred horizontally on a surface and get good homogeneity between surface-grained this reduces the surface defects of the models [22].

Table (3) shows the results obtained from the AFM screening compounds $Ni_{1-x}Cd_xFe_2O_4$ samples.

Samples	Roughness Average (nm)	Root Mean Square (nm)	Grain size (nm)
A	0.419	0.517	89.58
B	0.391	0.47	92.06
C	0.291	0.354	94.91
D	0.287	0.357	99.03
E	0.281	0.361	102.4
F	0.276	0.367	105.1

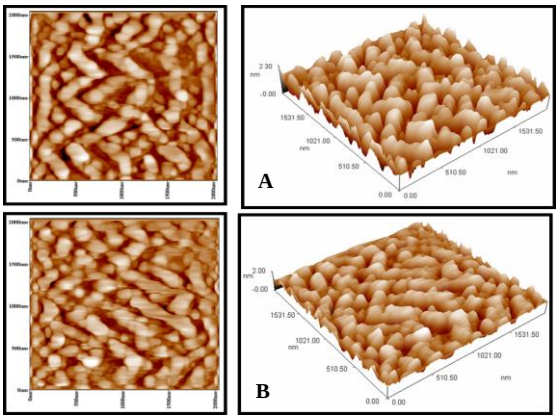

Fig.6 AFM micrograph show two-dimensional topographic analysis (2D) and three dimensions (3D) of A and B samples

The figure 7 (a-d), who shows the distribution of granular aggregates of the sample. It has been found that the rate of particle size increases with increasing values (x) this is consistent with the results of X-ray diffraction in that the granular size increases with the concentration of cadmium, but the rate of particle size measured by AFM is greater than the granular size measured by XRD and the reason for this is that AFM measures the particle size at which the sample surface while XRD measures the particle size within the model and the granules are larger at the surface than it is in the interior.

ISSN: 1813 – 1662 (Print)
E-ISSN: 2415 – 1726 (On Line)

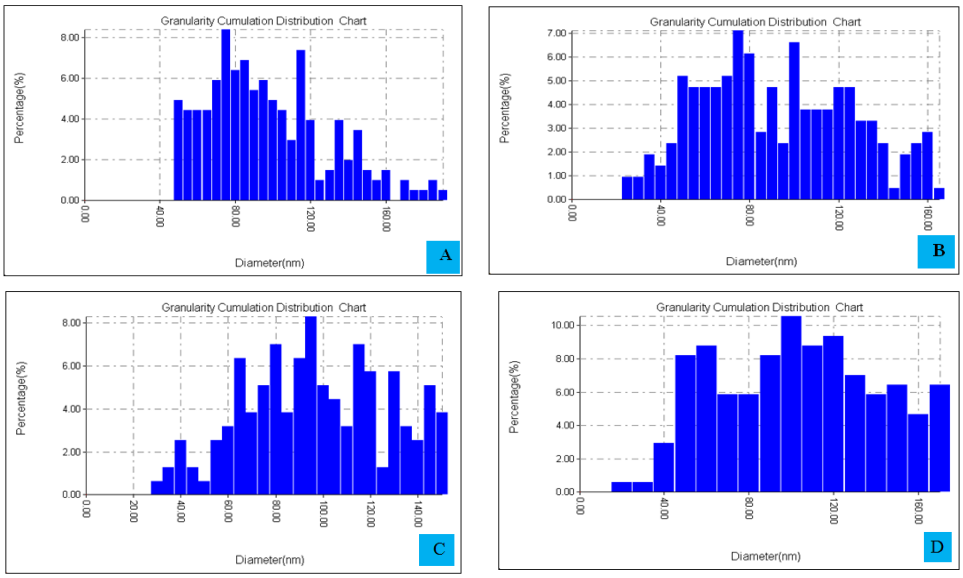

Fig. 7 (a-d) the distribution of granular aggregates of the A, B, C, and D samples.

3.3 The optical microscope

Shown in Figure 8(A-D) that the microstructure consists generally of iron floor basis with pale Algahoaia with nickel white granules dioxide and notes that the deployment be clear, but the lack of a strong correlation between the granular borders leading to the presence of some pores the cracks in the microstructure, which represents defects. The synthetic these defects have an impact on the physical properties of models Lafraatah. The figure 8(B) seems a more regular occurrence and homogeneous between the particles and this is due to the presence of cohesion between the granules cadmium, nickel, appearing in one piece, and that this regular distribution and homogenized increases with the concentration of cadmium as in Figure 8(C) and shape 8(D), leading to a strong cohesion between the granular border and this increases the movement, causing growth in grain size and thus less internal defects and surface in compositional structure which leads to improved mechanical properties and Alkahraiah as well as magnetic and this is consistent with the porosity results that have been reached it results from X-ray diffraction.

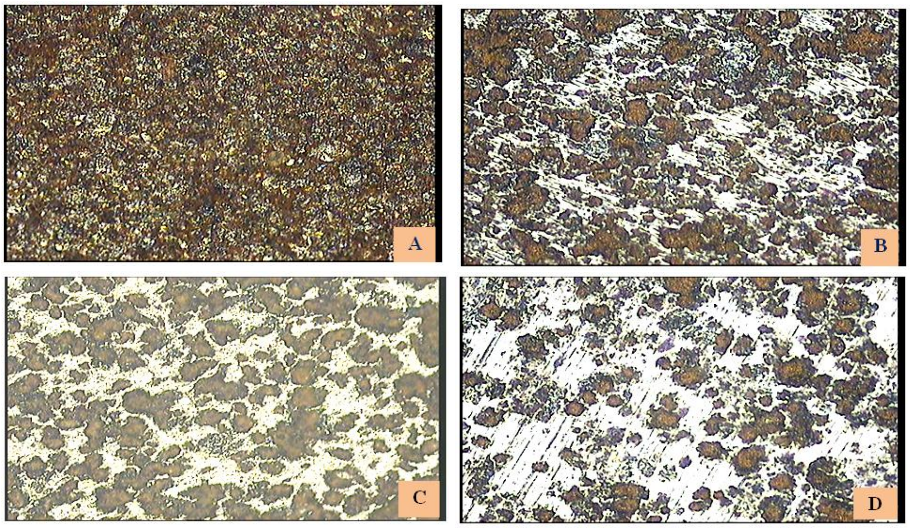

Fig. 8 The optical micrographs of A, B, C, and D samples

3.4 Dielectric Properties

1) Frequency dependent variation

The effect of frequency on dielectric constant (ε) at room temperature for all samples is illustrated in Fig. 9. From Fig. 9, it is clear that dielectric constant decreased with increasing frequency and finally at higher frequencies attains almost constant value for all the samples. This is obvious because of the fact that the species contributing to the polarizability are lagging behind the applied field at higher frequency. The variation of dielectric constant with frequency reveals the dispersion due to Maxwell-Wagner [23,24] type interfacial polarization, which is agreement with Koop's phenomenological theory [25]. The large values of dielectric at lower frequency are mainly due to presence of all type of polarization i.e. $P_{total} = P_e + P_i + P_d + P_{sc}$ where subscripts indicate the electronic, ionic, dipolar and space charge

contributions respectively. According to Sarah et al [26], the polarization in ferrites is through a mechanism similar to the conduction process. The exchange of electrons between ferrous ions (Fe^{2+}) and ferric ions (Fe^{3+}) on the octahedral site may lead to local displacement of electrons in the direction of applied field and these electrons determine the polarization. The polarization decreased with increasing frequency and then reaches a constant value due to the fact that beyond a certain frequency of external field the electron hopping cannot follow the alternating field. The AC resistivity is decreased with increasing in frequency at room temperature. Also it clears from Fig.10 that the AC resistivity in Ni-ferrite varies with the Cd-concentration which is in fair agreement with the conduction mechanism in ferrite. It is explained on the basis of hopping of charge carriers between the Fe^{2+} and Fe^{3+} ions on the octahedral site [27].

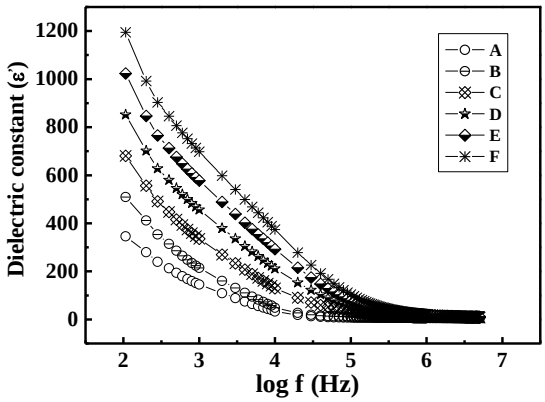

Fig. 9 Frequency dependent variations of dielectric constant for Ni-Cd ferrite samples

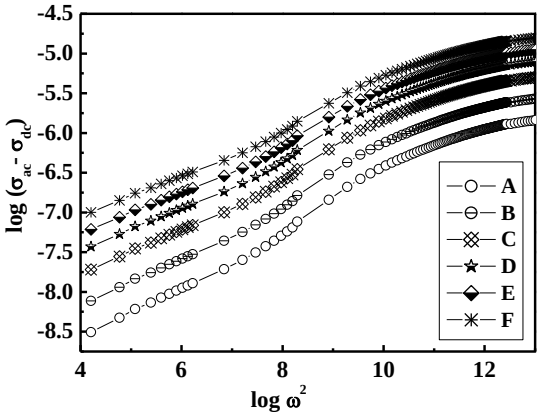

Fig. 10 Frequency dependent variations of AC conductivity for Ni-Zn ferrite samples

3.5 Hall-Effect

The resistivity was found to increase with Cd content due to the decrease in charge mobility. This may suggest that the resistivity here is mainly governed by charge carrier mobility rather than carrier concentration. The results of holes coefficient listed in Table 4 showed a p-type semiconductor behavior. Then the conduction mechanism in this ferrite is hopping of electrons between, $Fe^{3+}$and Fe^{2+}ions and hopping of halls between Ni^{3+} and Ni^{2+} which is the dominant one. The number of hopping of holes between Ni^{3+} and Ni^{2+} ions increases with Cd^{+3}doping. This is because of Fe^{3+} ions migration from the octahedral to the tetrahedral sites. The decrease in Hall mobility with Cd addition can be attributed to the restrictions in the lattice by the large Cd^{3+} doping ions [28, 29].

Table 4: Cd content effect on Hall mobility, sheet concentration, Resistivity, conductivity and Hall coefficient.

Samples	Sheet concentration [/cm^3]	Mobility [cm^2/v.s]	Resistivity [Ohm.cm]	Magneto-resistance [Ohm]	Conductivity [1/Ohm.cm]	Average hall coefficient [m^2/C]
A	$5.159*10^{+6}$	$2.75*10^{+3}$	$4.39*10^{8}$	$1.741*10^{9}$	$2.275*10^{-9}$	$1.2*10^{11}$
B	$7.076*10^{+7}$	$1.51*10^{+3}$	$1.16*10^{8}$	$1.03*10^{9}$	$8.611*10^{-9}$	$1.7*10^{10}$
C	$2.843*10^{+6}$	$1.33*10^{+3}$	$1.36*10^{8}$	$3.22*10^{9}$	$7.221*10^{-10}$	$6.5*10^{11}$
D	$5.057*10^{+6}$	$2.75*10^{+2}$	$1.17*10^{9}$	$8.61*10^{9}$	$5.173*10^{-10}$	$1.3*10^{10}$
E	$6.956*10^{+7}$	$1.95*10^{+2}$	$4.83*10^{9}$	$4.11*10^{9}$	$5.377*10^{-10}$	$3.4*10^{10}$
F	$6.573*10^{+7}$	$2.51*10^{+2}$	$2.73*10^{9}$	$4.03*10^{9}$	$6.113*10^{-10}$	$5.1*10^{11}$

3.6. Magnetic properties:-

Typical magnetic hysteresis loops for $Ni_{(1-x)}Cd_xFe_2O_4$ ferrites where x = 0, 0.1, 0.2, 0.3, 0.4 and 0.5 are shown in Fig. 11. It is clear that the saturation magnetization (M_S) increases with increasing Cd-concentration. The increase in saturation magnetization may be primarily due to the substitution of nonmagnetic Cd ion (d^{10}) for Co into the magnetic ferrite lattice. Cd^{+2} has a stronger preference for the tetrahedral site (A site), while Ni^{+2} ions (for which Cd is substituted) are located on octahedral site (B site) of AB_2O_4 spinel ferrite. Thus, Cd displaces Fe^{3+} from A to B site. As the magnetic spin of neighboring A and B sites are anti-ferromagnetically coupled (due to the super exchange interaction in ferrite lattice), the net result is an increase in magnetic moment on B sub-lattice, as well as the increase of the net magnetic moment of the crystal [30], while the value of H_c decreases with increasing Cd-content, which may be due to that the particle size is less than the critical size of single domain. In this range of particle size, the Hc variation

dependence on the particle size can be explained by Stoner-Wohlfarth theory [31]. According to the theory, the coercivity (H_c) of a single domain particle is $H_c = 2K/\mu_o M_s$, where K is the magnetocrystalline anisotropy constant, μ_o is the universal constant of permeability in free space and M_s is the saturation magnetization of the particles. The increase of Cd content results in complete crystallization, hence the value of K decreases, while M_s increases with increasing the particle size, so the variation of K and M_s seems to contribute to the corresponding H_c decrease in accordance with Fig. 11.

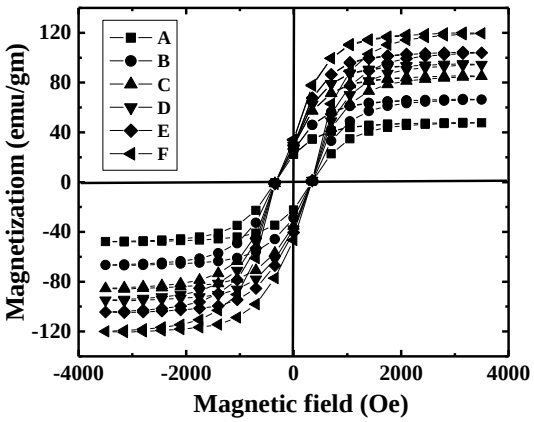

Fig. 11 Hysteresis of A, B, C, D, E, and F samples

4- Conclusions

1) In the present work, we have successfully synthesized $Ni_{x-1}Cd_xFe_2O_4$ ferrites by solid state reaction method.

2) In the structural study of Ni-Cd ferrites, crystalline nature is confirmed by X-ray diffraction. The Bragg's peaks observed in XRD plots are matching with the JCPDS data which indicates that the materials formed are of single phase having inverse spinel cubic structure. Also lattice constant, particle size and density are determined from XRD which agree with the theoretical data.

3) The room temperature Mossbauer spectra for all samples indicate the ferromagnetic nature of the prepared samples at room temperature.

4) Atomic force micrographs of Ni-Cd ferrites also show the average grain size around 89.58 – 99.03 nm.

5) The dielectric behaviour is explained in terms of electron exchange between Fe^{2+} and Fe^{3+}, suggesting that the polarization due to heterogeneity of the samples.

6) The AC conductivity measurements are useful to understand the thermally activated conduction mechanism and type of polarons responsible for conduction. The linearity of plot log ($\sigma_{ac} - \sigma_{dc}$) vs. log ω^2, confirms small polaron type of conduction and the slight change in conductivity is attributed to mixed polaron conduction.

7) The results of Hall coefficient showed a p-type semiconductor behavior.

8) The magnetic properties of $Ni_{1-x}C_XFe_2O_4$ ferrite are strongly affected by Cd content. The saturation magnetization increase with increasing the Cd content.

Acknowledgements

Author, A. F. Aziz wishes to thanks Tikrit University – Natural Ressources Research Center and the department of physics, university of pune - India for providing me the financial support during the course of my research.I'm thankful to the non-teaching staff of the department of physics, Mr. Valimble for their help and co-operation.

References

[1] Mahuya chakrabarti, D. Sanyal and A. Chakrab, J. Phys. Condens. Mater. 19 (2007) 11.

[2] A. S. M. Hudson, Marcani Review 1 (1970) 55.

[3] S. Kameoka, T. Tanabe, A.P. Tsai, Appl. Catal. A Gen., 375 (2010) 163-171.

[4] G. V. Duong, N. Hanh, D. V. Linh, R. Groessing, P. Weinberger, E. Schafler and M. Zehetbauer. J. Magn. Magn. Mater. 491 (2019) 431.

[5] V. Raghavan., "Materials Science and Engineering" (2006).

[6] C. Hammond,"The Basic of Crystallography and Diffraction" Oxford University Press, Oxford (2001).

[7] C. Duran, S. T. McKinstry and G. L. Messing. J. Electroceram. 10 (2003) 47.

[8] Xiwei Qi, Ji Zhou, Baorang Li, Yingchun Zhang, Zhenxing Yue, Zhilun Gui, and Longtu Li, J. Am. Ceram. Soc., 87 (2004) 1848.

[9] A. D. Sheikh and V. L. Mathe., J. Mater. Sci. 43 (2008) 2018.

[10] S. K. Kulkarni, Nanotechnology: Principles and practices" (2007).

[11] Pramod K Sharma, Z Ounaies, V V Varadan and V K Varadan, Smart Mater. Struct. 10 (2001) 878-883.

[12] L. S. Deshmukh, K. Krishnakumar, S. Balakrishna, A. Ramakrishna and G. Sasathaiah., Bull. Mater. Sci. 21 (1998) 219.

[13] C. B. S. Tower, Rochelle Salt as a Dielectric. Physical Review, 35 (1930) 265.

[14] P. K. Roy, J. Bera, J. Magn. Magn. Matter. 321 (2009) 247-251.

[15] N. H. Vasoya, V. K. Lakhani,P. U. Sharma, K. B. Modi, RAVI Kumar and H. H. Joshi, J. Phys. Condens. Matter 18 (2006) 8063-8092.

[16] H. E. Zhang, B.F. Zhang_, G.F. Wang, X.H. Dong, Y. Gao, J. Mag. Mag. Mater. 312 (2007) 126.

[17] Abdulsamee, A. D. Sheikh and V. L. Mathe. Journal of Alloys and compounds, 502 (2010) 231-237.

[18] A. M. Abdeen, O. M. Hemeda, E. E. Assem, and M. M. El-Sehly, J. Magn. Magn. Mater. 238 (2002) 75-83.

[19] Mahuya Chakrabarti, D Sanyal and A Chakrabarti, J. Phys.; Condens Matter. 19 (2007)

[20] [C.Otero Arean, E. Garcia Diaz, J.M. Rubio Gonzalez, M.A. Villa Garcia, J. Solid State Chem., 77 (1988) 275-280
[21] B. Viswanathana and V. R. K. Murthy, Ferrite Materials–Science and Technology, Narosa Publishing house, New Delhi (1980).
[22] Jasmeen Saini, Rupesh Kumar, Jaspreet Kaur Rajput, Arvind Kumar, International Journal Of Engineering And Computer Science 4 (2015)11032-11036.
[23] J. C. Maxwell, Electricity and Magnetism (Oxford University, Press, London, 1973).
[24] K. W. Wagner, Ann, Physik, 40 (1993) 818.
[25] C. G. Koops, Phys. Rev., 83 (1951) 121.
[26] Y.H. Tang, X.M. Chen, Y.J. Li, X.H. Zheng. Mater. Sci. Engg. B 116 (2005) 150.
[27] I. G. Austin and N. F. Mott Adv. Phys. 18 (1996) 411.
[28] Muthafar F. Al-Hilli, Iraqi Journal of Physics, 9 (2011) 6-12.
[29] Douaa Basil, Muthafar F. Al- Hilli, Farah T. Muhammed Noori Iraqi Journal of Physics, 11 (2013) 102-109.
[30] M. M. Mallapur, M. Phil. Dissertation, Shivaji Univ., Kolhapur (2003).
[31] Jing-Jiang, Yan-Min Yang, Liang-Chao Li, Physica B 399 (2007) 105-108.

" تركيب وطيف موزبير والخواص المغناطيسية لمركبات $Ni_{(1-x)}\ Cd_x\ Fe_2O_4$ المحضرة بطريقة تفاعلات الحالة الصلبة"

عبدالسميع فوزي عبدالعزيز البياتي

مركز بحوث الموارد الطبيعية ، جامعة تكريت ، تكريت ، العراق

الملخص

تم تحضير مسحوق فرايت النيكل – كادميوم ذات الصيغة الكيميائية $Ni_{1-x}Cd_xFe_2O_4$ حيث ان$0 \leq X \leq 0.5$ وذلك باستخدام طريقة تفاعلات الحالة الصلبة. حيث اظهرت نتائج حيود الاشعة السينية بأن جميع النماذج ذات الطور الأحادي ذو تركيب بلوري مغزلي الشكل مع زيادة ثابت الشبيكة والكثافة مع زيادة تركيز الكادميوم مع نقصان في المسامية. تم حساب الحجم الجبيبي من دراسة حيود الاشعة السينية. صلادة فيكرز لنظام فيرايت النيكل– كادميوم تتغير من532 الى 586.6. ان الزيادة الحاصلة في صلادة المركبات ناتجة عن زيادة تركيز الكادميوم. كما تبين زيادة الحجم البلوري مع زيادة تركيز الكادميوم باستخدام تقنية مجهر القوة الذري. كما تم دراسة تغير كل من ثابت العزل الكهربائي, ظل الفقد والتوصيلية المتناوبة مع التردد عند مدى تردد (100 Hz – 5 MHz). حيث اظهرت الدراسة ان ثابت العزل الكهربائي يقل مع زيادة التردد لجميع النماذج مع تحقق استقطاب ماكسويل ويكنر. اما دراسة تاثير معامل هول يبين ان جميع النماذج موجبة اي ان حاملات الشحنة الاغلبية من نوع (p). أما نتائج الفحوصات المغناطيسية لفرايت$Ni_{(1-x)}\ Cd_xFe_2O_4$ يتأثر بتركيز الكادميوم بشكل كبير. اما ظاهر موزبير تبين التركيب البرمي لجميع النماذج.

الكلمات المفتاحية: حيود الاشعة السينية ، المجهر الالكتروني ، ثابت العزل الكهربائي ، حلقة الهسترة.